Völksch, I., Schwank, M., Mätzler, C. (2011): L-Band Reflectivity of a Furrowed Soil Surface. - IEEE Transactions on Geoscience and Remote Sensing, 49, 6, 1957-1966

DOI: 10.1109/TGRS.2010.2091720

L-Band Reflectivity of a Furrowed Soil Surface

Ingo Völksch, Mike Schwank, and Christian Mätzler, *Senior Member, IEEE*

***Abstract*—In a combined experimental and model study, we investigated the thermal L-band signatures of a sandy soil with periodic topography (furrows) with dimensions close to the observation wavelength of 21 cm. Measurements were carried out with a radiometer mounted on a tower and aimed at a soil box with an artificially prepared furrowed soil surface. Corresponding reflectivities were derived from brightness temperature measurements performed under dry and moist conditions, with the furrow direction either along or perpendicular to the plane of incidence. Results showed that the furrows had a pronounced effect on the reflectivity, depending on the polarization of the observed radiance, the direction of the furrows, and the soil moisture. A physical reflectivity model for dielectric periodic surfaces was used to explain the soil reflectivities measured for the different furrow directions and soil-water contents. Using this model improved the agreement between the measured and modeled reflectivities considerably compared to the Fresnel reflectivities. The observed dependence of soil reflectivity on furrow orientation and soil moisture could be reproduced by the reflectivity model. The quantitative agreement with the observed reflectivities was further improved by using a simple empirical approach to consider the small-scale heterogeneity of the top soil layer.**

***Index Terms*—Electromagnetic scattering by periodic structures, electromagnetic scattering by rough surfaces, microwave radiometry, permittivity.**

I. Introduction

THE TERRESTRIAL surface layer is one of the major components of the climate system. Mass and energy fluxes at the earth's surface control how energy received from the sun is returned to the atmosphere, thus influencing the climate considerably. The quantities involved in this mass and energy exchange are fundamentally linked with the moisture in the soil surface. For example, soil moisture strongly controls infiltration processes and the amount of water dissipated to the atmosphere via evaporation and transpiration. Therefore, it is crucial to know how much water is stored in the top soil layer in order to understand the processes that link the terrestrial water and energy cycles.

Manuscript received April 11, 2010; revised August 24, 2010; accepted November 3, 2010. Date of publication January 16, 2011; date of current version May 20, 2011. This work was supported by the Swiss National Science Foundation (SNF) under Grant 200021-112151.

I. Völksch is with the WSL Swiss Federal Institute for Forest, Snow and Landscape Research, 8903 Birmensdorf, Switzerland (e-mail: ingo.voelksch@wsl.ch).

M. Schwank was with the WSL Swiss Federal Institute for Forest, Snow and Landscape Research, 8903 Birmensdorf, Switzerland. He is now with the German Research Centre for Geosciences (GFZ), 14473 Potsdam, Germany (e-mail: mike.schwank@gfz-potsdam.de).

C. Mätzler, retired, was with the Institute of Applied Physics, University of Bern, 3012 Bern, Switzerland (e-mail: christian.matzler@iap.unibe.ch).

Digital Object Identifier 10.1109/TGRS.2010.2091720

Almost 30 years ago, it was suggested that soil moisture could be retrieved from remotely sensed thermal radiance measured with an L-band (1–2 GHz) microwave radiometer [1], [2]. Today, L-band radiometry is one of the most promising approaches for remotely monitoring soil moisture on a large scale. It has the advantage of being unaffected by cloud cover and solar radiation, which allows all-weather continuous (day and night) measurements. Furthermore, the emission depth in soils is relatively large, and the vegetation canopy is semitransparent at L band. The sensitive 1400–1427 MHz frequency band of most L-band radiometers is protected, which means that disturbances due to anthropogenic interferences are minimized.

Microwave radiometry is also being deployed in the recently launched Soil Moisture and Ocean Salinity (SMOS) mission of the European Space Agency. The Microwave Imaging Radiometer using Aperture Synthesis that is onboard the SMOS satellite provides global coverage of L-band brightness temperatures with a spatial resolution of approximately 50 km. The primary objective of the mission is to produce global soil moisture maps with an accuracy better than 4 vol.% and ocean salinity maps with an accuracy of 0.5–1.5 practical salinity units [3]. The reliability of these data products depends largely on the performance of the emission models applied to interpret the brightness temperatures measured on the corresponding footprints. For this reason, a large number of ground-based (e.g., [4]) and airborne radiometer experiments (e.g., [5]) at L band over various types of terrestrial surfaces have been performed during recent decades.

It has been demonstrated that the brightness temperatures measured are affected not only by the surface moisture but also by other parameters such as soil roughness and topography. This finding has led to extensive research on the impact of random surface roughness on the signatures measured (e.g., [6]–[9]). However, a periodic topography of a soil surface can also affect the thermal microwave signatures [10], [11]. Examples of such terrestrial surfaces are soils undergoing erosion and dispersal processes, which can produce gullies preferentially aligned with the slope. Agricultural fields may also have pronounced periodic structures, particularly furrows produced as a result of, e.g., plowing, sowing, or furrow irrigation.

Extensive experimental and theoretical investigations have been dedicated to the emission properties of periodic surfaces in the context of L-band brightness temperature measurements over the surface of the sea. Knowing these properties made it possible to correct for wind effects in sea salinity retrievals [12]. Moreover, correlations between wind direction and the characteristics of the formed periodic surface waves can be used to retrieve wind direction [13]. Although the theoretical background is available (e.g., [14] and [15]), to our knowledge, not many experimental studies have been dedicated to the

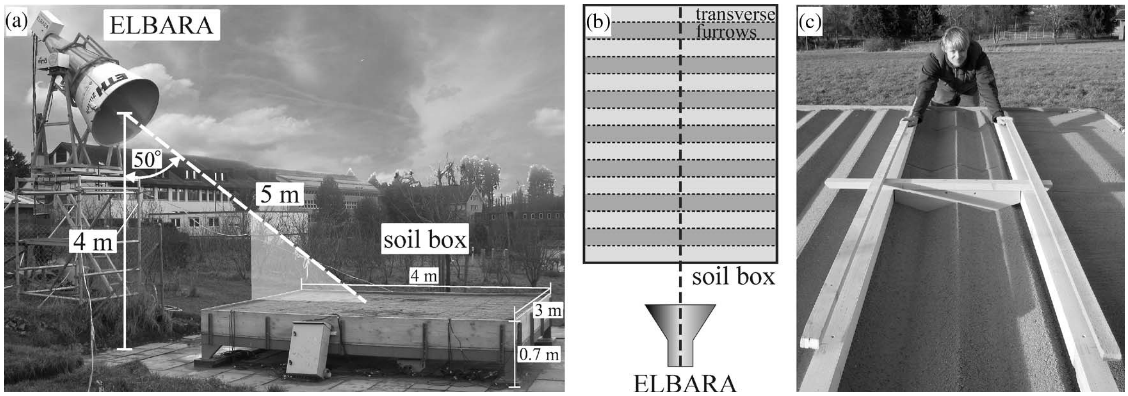

Fig. 1. (a) Setup of the experiment. The dashed line is the antenna main axis; the shaded area illustrates the plane of incidence. (b) Sketch of the setup as seen from above with transverse furrows (i.e., furrow orientation perpendicular to the plane of incidence) imprinted into the soil surface. (c) Preparation of the furrowed surface.

thermal emission of soils with periodic surface features in the range of the observation wavelength.

To investigate the thermal emission of a soil with a well-defined 1-D periodic topography, parallel furrows with a periodicity of $\approx$27 cm were imprinted into a bare soil surface. Brightness temperatures at 1.4 GHz were then measured under dry- and moist-soil conditions for a soil with furrows either aligned with or perpendicular to the plane of incidence (Section II). For comparison, smooth soil surfaces were also measured under each moisture condition. From the brightness temperatures measured, the corresponding reflectivities were derived (Section III-A) to investigate the impact of periodic topography on the soil reflectivity for the different furrow orientations and soil moistures. As the observation wavelength ($\lambda \approx 21$ cm) was similar to the surface periodicity, a physical reflectivity model (Section III-B) was implemented to explain the topography-related aspects of the signatures measured. Modeled values were then additionally corrected for further effects not accounted for in the physical reflectivity model (e.g., small-scale heterogeneity of the top soil layer) with a simple empirical approach (Section III-D). The reflectivity changes caused by the differently oriented furrows under dry- and moist-soil conditions are discussed on the basis of the measurements and the corresponding model calculations in Section IV.

II. Experiment

Measurements were performed with the ETH L-Band Radiometer (ELBARA) [16] at the Swiss Federal Research Institute WSL in Birmensdorf (Switzerland) in January 2008 (Fig. 1). A soil box was placed in ELBARA's footprint, and brightness temperatures were measured for three different soil topographies under dry- and moist-soil conditions. The experimental setup, the remote sensing system, and the measurements performed are described in more detail in the following.

A. Setup

ELBARA was mounted on a small tower with the observation angle $\theta = 50^\circ$ relative to the vertical direction and the antenna aperture approximately 4 m above the ground [Fig. 1(a)]. An area of about 5 m $\times$ 8 m in the radiometer footprint was leveled and paved with concrete slabs to achieve a horizontal and even surface. The paving covered at least the -12 dB footprint of ELBARA. It was ascertained experimentally that radiation emitted by the grassland surrounding the paving did not affect the signatures measured.

The 3 m $\times$ 4 m $\times$ 0.3 m soil box (made of 3 cm wooden planks mounted on top of a steel frame) was placed in the center of the paved area with its long sides aligned with the plane of incidence. It was filled with sandy soil from the research catchment "Chicken Creek" [17]. Prior to this, the soil was sieved to remove clumps of soil particles larger than 5 mm, resulting in a homogenous sandy soil (soil texture: 88% sand, 7% silt, and 5% clay) with a density of 1535 $\mathrm{kg \cdot m^{-3}}$ and a porosity of approximately 25%. When filling the box, a layer of moist soil was placed at the bottom and gradually drier soil was added on top. This resulted in a rather smooth soil moisture profile, with the soil-water content wc decreasing from $\approx 0.2\ \mathrm{m^3 \cdot m^{-3}}$ at the bottom of the soil box to $\approx 0.01\ \mathrm{m^3 \cdot m^{-3}}$ in the top soil layer. The power penetration depth of the moist soil with $wc = 0.2\ \mathrm{m^3 \cdot m^{-3}}$ was estimated as $\lambda/(4\pi \mathrm{Im}\sqrt{\varepsilon}) \approx 5$ cm, whereas $\lambda \approx 21$ cm is the observation wavelength, and $\varepsilon \approx 16 + i3$ is the relative permittivity of the soil (see Section III-C for the relationship between wc and ε of the soil investigated). This indicates that the radiance emitted from the pavement below could not permeate the soil box and interfere with the upward emission of the soil. Furthermore, the gradual moisture profile reduced coherent effects due to layering, which, however, cannot be ruled out altogether.

This setup with the shallow observation angle $\theta = 50^\circ$ and the small distance of $\approx$5 m between the antenna aperture and the observed scene was chosen as a compromise. On the one hand, it ensured that the self-radiation of the antenna reflected back toward the antenna aperture was negligible, while on the other hand, the footprint area was kept very confined so that the measured signatures were largely determined by the soil-box reflectivity. The observed scene was still within the near field of the antenna with this setup. Therefore, the fractional contribution of the soil-box radiance to the total radiance received could not be estimated using the theoretical antenna far-field pattern [18]. Instead, we determined this quantity experimentally, as described in Section III-A.

B. Instrumentation

The L-band radiometer ELBARA [16] was constructed at the Institute of Applied Physics, University of Bern (Switzerland), in 2001 and has been successfully deployed in numerous experiments since then [19]–[25]. It is equipped with a dual-mode Picket-horn antenna [18] (aperture diameter $d = 1.4$ m, length $l = 2.7$ m) with a gain of 23.5 dB and a -3 dB full beamwidth of 12°. ELBARA measures brightness temperatures T_{B}^{p} at horizontal ($p = \mathrm{H}$) and vertical ($p = \mathrm{V}$) polarization in the protected frequency band 1400–1427 MHz ($\lambda \approx 21$ cm). Two slightly overlapping frequency channels, each with a bandwidth of 18 MHz (1400–1418 and 1409–1427 MHz), are measured quasi-simultaneously to enable the detection of narrow-band radio frequency interference (RFI) within the protected band. As no disturbances due to RFI were encountered during the measurements, the brightness temperatures associated with the two channels were averaged to use the total bandwidth of 27 MHz. The measurements were recorded with 12 s integration time, yielding a large time–bandwidth product. The estimated absolute accuracy of the T_{B}^{p} measured was ± 1 K, and the sensitivity was better than 0.1 K. The measured T_{B}^{p}'s were corrected for the radiance originating from the cables connecting the antenna with the radiometer electronics by comparing the measured sky brightness $T_{\mathrm{B,sky}}$ with the values calculated with [26] and then correcting the measurements accordingly as described in [27].

In addition to the radiometer measurements, air and ground temperatures were also measured. Air temperature T_{air} was recorded with a shaded Pt-100 temperature sensor installed on the radiometer scaffolding, and *in situ* soil temperatures $T_{18\,\mathrm{cm}}$ were measured with three thermistors (Campbell S-TL107) buried in the soil along a transect at a depth of 18 cm. The accuracy of these temperature measurements was approximately ± 1 K. $T_{18\,\mathrm{cm}}$ and T_{air} were used to estimate the effective temperature T_{s}, which predominantly determines T_{B}^{p} (Section III-A).

C. Measurements

Brightness temperature measurements were performed on January 10 and 19, 2008. Both days were dry, sunny, and unseasonably warm, with mean air temperatures during the measurements of 12 °C and 13 °C, respectively. Mild and rainy weather prevailed between the two days of measurements, resulting in natural wetting of the sandy soil. On January 10 (dry-soil measurements), the near-surface soil-water content was determined to be $wc = 0.014\ \mathrm{m}^3 \cdot \mathrm{m}^{-3}$ from soil samples taken from the surface layer (approximately the topmost 5 cm). On January 19 (moist-soil measurements), wc ranged from 0.067 to 0.094 $\mathrm{m}^3 \cdot \mathrm{m}^{-3}$.

Three different types of surface topography were prepared for the T_{B}^{p} measurements: 1) a surface with periodic furrows parallel to the plane of incidence (*longitudinal furrows*); 2) a surface with periodic furrows perpendicular to the plane of incidence [*transverse furrows*, shown in Fig. 1(b)]; and 3) a *plane surface* (i.e., a smoothed surface without furrows). The plane surface was prepared by pulling a board back and forth over the soil until the surface was very smooth. This resulted in a surface with reflection characteristics that were as close to specular (Fresnel) reflection as was experimentally feasible.

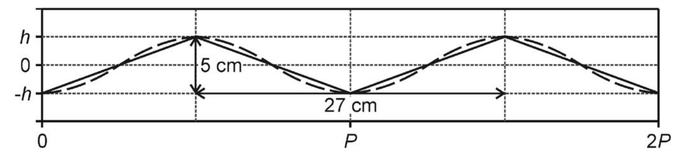

Fig. 2. Illustration of the cross section of the prepared furrows (solid line) and its mathematical representation in the reflectivity model (dashed line).

The furrowed surfaces were prepared from plane surfaces by pulling a wooden stencil formed like a triangular snow plow through the soil [Fig. 1(c)] in either a longitudinal or a transverse direction. The cross sections of the longitudinal and the transverse furrows were identical and can be described as an isosceles triangle with an altitude of 5 cm, side lengths of ≈15 cm, and a base length of ≈27 cm, corresponding to the period P of the furrows (Fig. 2). This geometry was chosen to resemble "natural" structures such as irrigation or plowing furrows to some degree while at the same time being experimentally feasible and well defined. The smoothness of the furrow faces was approximately the same as the smoothness of the plane surface.

During both the dry- and moist-soil measurements, the soil topography was changed in the following order: 1) plane surface; 2) surface with longitudinal furrows; 3) plane surface; 4) surface with transverse furrows; and 5) plane surface. For each soil topography 1) to 5), T_{B}^{p}'s were measured 20 times, and two soil samples were taken randomly from the top soil layer, from which wc was determined gravimetrically in the laboratory. Afterward, the next topography was prepared, and the procedure was repeated in the same way.

These measurements resulted in a data set of T_{B}^{p} for the plane and for the two furrowed soil surfaces at different wc. The three measurements, namely, 1), 3), and 5), of the plane surface under dry and moist conditions provided a reference, which helped to distinguish the T_{B}^{p} variations due to the different topographies from the changes caused by varying wc.

III. Models

Reflectivities R^p of the soil under test were derived from the T_{B}^{p} measurements of the soil box placed in the footprint using the radiative-transfer model described in the following. These *measured* reflectivities were then compared to *modeled* reflectivities, computed with the physical reflectivity model for dielectric periodic surfaces outlined in Section III-B. The soil-water content wc is taken into account through the relative permittivity ε of the soil, which is linked to wc. Section III-C presents the experimentally derived relationship between wc and ε for the sandy soil used in this study. The modeled reflectivities were later corrected for effects not considered in the physical reflectivity model using the simple empirical approach described in Section III-D.

A. Radiative Transfer

The measured brightness temperatures T_{B}^{p} ($p = \mathrm{H, V}$) are a composite of the radiances emitted from the soil box and from the surroundings. This is considered in the radiative-transfer model (1), which describes T_{B}^{p} as the linear combination of the soil-box radiance and the radiance of the surrounding paved area. These contribute with the fractional amounts μ^p and $(1-\mu^p)$, respectively. The corresponding reflectivities are the reflectivity R^p of the soil under test and the reflectivity R_0^p of the paving, whereas a uniform effective ground temperature T_s is assumed for both areas. With $T_{\mathrm{B,sky}} \approx 5$ K [26] being the sky brightness, this yields

$$T_\mathrm{B}^p = \mu^p \left[(1-R^p)T_\mathrm{s} + R^p T_{\mathrm{B,sky}}\right] + (1-\mu^p)\left[\left(1-R_0^p\right)T_\mathrm{s} + R_0^p T_{\mathrm{B,sky}}\right]. \qquad (1)$$

This zero-order radiative-transfer model fulfills Kirchhoff's law. Furthermore, the terms $(1-R^p)$ and $(1-R_0^p)$ express the emissivities of the soil under test and the paved area, respectively, if thermodynamic equilibrium is assumed.

Similar to the parameterization proposed in [28], T_s was estimated as the mean of the air temperature T_air and the ground temperature $T_{18\,\mathrm{cm}}$. This approximation might deviate somewhat from the unknown true value of the effective ground temperature. However, its temporal variation is assumed to be synchronous to that of the true T_s. The reflectivities $R_0^\mathrm{H} = 0.38$ and $R_0^\mathrm{V} = 0.13$ of the paving were derived from $T_\mathrm{B}^p = (1-R_0^p)T_\mathrm{s} + R_0^p T_{\mathrm{B,sky}}$ measured before the soil box was placed in the radiometer footprint [25]. The values for μ^p were estimated from brightness temperatures $T_{\mathrm{B,mesh}}^p$ measured for the soil box covered with a reflector (aluminum mesh with mesh size ≈2 mm). Inserting $T_{\mathrm{B,mesh}}^p$ together with $R_{\mathrm{mesh}}^p = 1$ and the previously determined R_0^p in (1) and solving for μ^p yielded $\mu^\mathrm{H} = 0.71$ and $\mu^\mathrm{V} = 0.81$. The difference between μ^H and μ^V is attributed to the polarization-dependent reflectivity of the wooden board of the box facing the radiometer, which was not covered with the reflector during the $T_{\mathrm{B,mesh}}^p$ measurements.

With all the quantities in (1) except for the soil reflectivity R^p known, R^p can be derived from the T_B^p measured with

$$R^p = \frac{T_\mathrm{B}^p - T_\mathrm{s}}{\mu^p(T_{B,\mathrm{sky}} - T_\mathrm{s})} + \left(1 - \frac{1}{\mu^p}\right) R_0^p. \qquad (2)$$

B. Reflectivity of a Dielectric Periodic Surface

Models using full-wave electromagnetism are required to simulate the interaction of electromagnetic waves with dielectric structures featuring spatial periodicities in the range of the observation wavelength. In contrast to models based on physical optics (short-wavelength approximation) or geometric optics (which ignore wave effects), the full-wave electromagnetic approaches seek solutions for Maxwell's equations at the dielectric boundaries. An extensive theoretical overview can be found in, e.g., [14] and [15].

To explain certain aspects of the signatures measured for the periodic soil surfaces described in Section II, we implemented the reflectivity model presented in [15, Ch. 3]. This physical model solves Maxwell's equations for the electric and magnetic fields at a 1-D dielectric periodic surface using the extended boundary condition approach. This approach uses scalar functions for the surface fields, which are represented by their Fourier series expansion. The corresponding unknown Fourier coefficients are derived by solving the T-matrix equations (see [14, Ch. 2, Sec. 7]).

To simplify the evaluation of the model, the surface was assumed to be represented by a sinusoidal function with amplitude h and periodicity P perpendicular to the direction of the furrows, as shown in Fig. 2 (the surface is invariant along the furrow direction). Furthermore, the relative permittivity of the soil was assumed to be constant with depth. In that case, closed-form expressions for the T-matrix elements exist and can be expressed by using Bessel functions. Once the surface fields (actually their Fourier coefficients) are known, the fields scattered in discrete upward directions (Floquet modes) are computed. Finally, the reflectivity R^p of the sinusoidal surface is derived as the ratio between the power reflected per surface period and the corresponding incident power. The power reflected is expressed by summing up the powers carried by the Floquet modes propagating in an upward direction. This approach allows R^p of our furrowed surface (approximated as a 1-D sinusoidal surface with amplitude h and period P) to be computed for arbitrary elevation and azimuth angles of the incident wave with respect to the furrow direction. The period and amplitude were set to $P = 27$ cm and $h = 2.5$ cm, respectively, resulting in a sine function with the same periodicity and amplitude as the prepared triangular furrows (Fig. 2). Another feasible assumption would have been to choose h such that the sinusoidal surface features the same root-mean-square height as the prepared furrowed surface ($h \approx 2.0$ cm). Both options yielded similar results, whereas the choice of $h = 2.5$ cm gave the best overall agreement of model results with observations.

Implementation of this mathematically quite complex reflectivity model was time consuming and demanding. In order to forestall errors in the coding, the model was programmed independently in Mathematica, as well as in Matlab. Exemplary calculations yielded identical results for both implementations. To further validate the coding, the examples presented in [15] were recalculated and could be reproduced.

C. Soil Permittivity

The relation between the volumetric water content wc ($\mathrm{m}^3 \cdot \mathrm{m}^{-3}$) and the complex relative permittivity $\varepsilon = \varepsilon' + i\varepsilon''$ of the sandy soil used was determined experimentally. The resulting relation $\varepsilon(wc)$ was then used as input to the reflectivity model (Section III-B) to compute R^p for the different soil topographies at the different soil moistures wc, whereas wc was assumed to be constant with depth.

To derive $\varepsilon(wc)$, first, soil samples with wc between 0 $\mathrm{m}^3 \cdot \mathrm{m}^{-3}$ (oven dry) and 0.2 $\mathrm{m}^3 \cdot \mathrm{m}^{-3}$ (almost water saturated) were prepared. The corresponding ε was then measured at room temperature (23 °C) with a network analyzer (Hewlett Packard 8753 ES) and an attached coaxial chamber (diameter of the outer conductor: 60 mm, diameter of the inner conductor: 26 mm, length: 200 mm, volume: ≈470 cm^3) containing the respective soil sample. The frequency range measured was 0.1–2 GHz. In analogy to the empirical relation proposed in [29], a third-order polynomial equation was fitted to the real and imaginary parts of ε measured for 1.4 GHz

$$\begin{aligned} \varepsilon' &= 671.2wc^3 + 173.9wc^2 + 4.5wc + 2.66 \\ \varepsilon'' &= 603.2wc^3 - 88.9wc^2 + 8.2wc + 0.03. \end{aligned} \qquad (3)$$

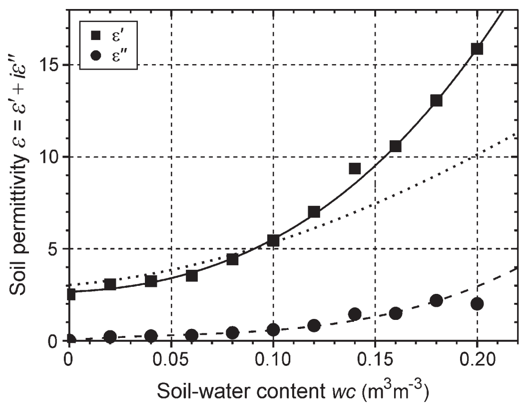

Fig. 3. Measured relationship between relative soil permittivity $\varepsilon = \varepsilon' + i\varepsilon''$ and soil-water content wc (solid symbols). The solid and dashed lines are the empirical best fit equations (3). For comparison, the empirical relation [29] is also shown (dotted line).

Fig. 3 shows the measured relationship $\varepsilon(wc)$, together with (3) and the empirical relation of [29]. It is apparent that the latter yields only poor results for the soil under test, whereas (3) fits the observations well. For the range $0\ \mathrm{m}^3 \cdot \mathrm{m}^{-3} < wc < 0.1\ \mathrm{m}^3 \cdot \mathrm{m}^{-3}$ observed during the radiometer measurements, the errors of the relations (3) are ≤ 0.23 for ε' and ≤ 0.05 for ε''. It is furthermore assumed that using the soil-specific relation (3) yields more accurate results than applying semiempirical dielectric mixing models, such as [30] or [31].

D. Correction for Heterogeneities Affecting Soil Reflectivity

The soil reflectivity can be affected by a number of additional factors besides the furrows, which are not accounted for in the reflectivity model outlined in Section III-B. On the one hand, small-scale surface roughness is superimposed on the prepared surfaces, and the top soil layer is expected to exhibit a certain heterogeneity due to the manipulation of the soil surface and due to drying in the course of the measurements. On the other hand, soil moisture (and thus soil permittivity) is assumed to be constant with depth in the reflectivity model, whereas in reality, the soil moisture increased with depth. Other factors are uncertainties in the effective soil temperature T_{s} and the deviation of the real cross section of the furrows from its mathematical representation in the reflectivity model (Fig. 2). Not least, it has to be noted that both the reflectivity model and the radiative-transfer approach (1) are based on the assumption of a fixed observation angle $\theta = 50^\circ$ for the entire observed scene, whereas in reality, the observed soil box covered local view angles ranging from approximately 40° to 60° as seen from the center of the antenna aperture.

As these factors cannot be quantified (measured) exactly and since our study focuses on the influence of surface topography on soil reflectivity, we applied a very simple empirical approach to account for these effects

$$R^{p*} = R^p \exp(-h^p). \tag{4}$$

That means that (uncorrected) reflectivities R^p $(p = \mathrm{H, V})$ were multiplied with an exponential correction function, yielding modified values R^{p*} corrected for the combination of the effects mentioned earlier. This single parameter correction can be seen as a simplified form of the roughness model proposed in [32]. It results from [32] when polarization mixing is assumed to be negligible which is a common practice when correcting passive L-band signatures for small-scale roughness [9], [33]. However, it is important to note that the model [32] and, even more, the relation (4) are empirical in nature, and therefore, no clear physical meaning should be associated with the empirical h^p parameter used in (4). Furthermore, h^p can be distinctly different for horizontal and vertical polarizations as a result of dielectric anisotropy in the air-to-soil transition zone [34], [35].

The values of h^p were obtained by minimizing the cost function $CF(h^p)$ representing the sum of the squared differences between the modified R^{p*} and the corresponding observations R^p

$$CF(h^p) = \sum (R^{p*} - R^p)^2. \tag{5}$$

This approach simply adapts model results to observations empirically. This yields rather good results when applied in addition to the physical reflectivity model, as will be shown in Section IV-C.

IV. Results and Discussion

In Section IV-A, we present the results of the measurements and the model simulations. The impact of the furrows on the measured and modeled soil reflectivities is further discussed in Section IV-B on the basis of the relative reflectivity changes (relative to the plane surface reflectivity) caused by the furrows. Since both sections focus on the influence of the surface topography on the soil reflectivity, only the (uncorrected) simulations performed with the physical reflectivity model (Section III-B) are considered. The modeled reflectivities, corrected with the approach introduced earlier, are shown in Section IV-C, where the model performance is discussed.

A. Reflectivities

Fig. 4 shows the results of the measurements (solid symbols) and the model simulations (empty symbols). The measured and modeled reflectivities R^p at horizontal (squares) and vertical polarization (circles) are shown for the different soil topographies and soil moisture conditions investigated. Panel (a) shows the results for dry soil, and panel (b) shows those for moist soil.

The measured R^p's were derived from the measured brightness temperatures T_{B}^p using (2). The mean values of the 20 measurements performed for each surface type are given. Since the associated standard deviations were very small (≤ 0.003) in all cases, no uncertainty ranges are shown. The modeled R^p's for the different surface topographies and soil moistures were computed with the physical reflectivity model. The necessary soil permittivity $\varepsilon(wc)$ was determined from the measured near-surface soil-water content wc using (3). The error bars in panel (b) represent the range of R^p resulting from using the highest and lowest values of the ten wc observations made during the moist-soil measurements. This illustrates the uncertainty in R^p modeled due to the temporal and spatial variation of wc observed on that day. No error bars are shown in panel (a) since wc of the soil-surface layer was constant throughout the dry-soil measurements.

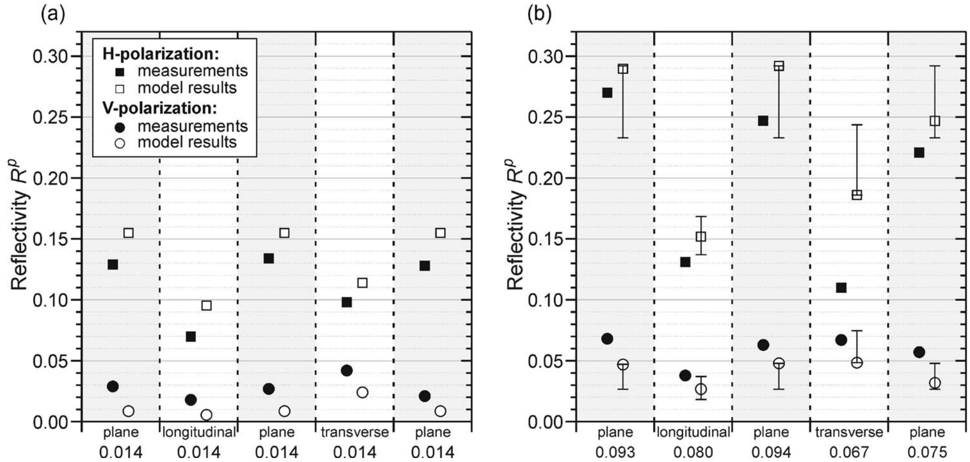

Fig. 4. Measured (solid symbols) and modeled (empty symbols) reflectivities R^p $(p = \mathrm{H, V})$ of the different surfaces at horizontal (squares) and vertical polarization (circles). The abscissa labels indicate the different surface topographies (plane surface, longitudinal furrows, and transverse furrows) and the corresponding *in situ* measured soil-water contents wc $(\mathrm{m}^3 \cdot \mathrm{m}^{-3})$. Panel (a) is for dry soil, and panel (b) is for moist soil. Plane surface measurements are highlighted in gray for the sake of clarity.

1) Dry-Soil Measurements [Fig. 4(a)]: All three measurements of the plane dry-soil surface at $p = \mathrm{H}$ yielded $R^{\mathrm{H}} \approx 0.13$. With longitudinal furrows, R^{H} decreased almost by half with respect to the plane surface to $R^{\mathrm{H}} \approx 0.07$. Transverse furrows also decreased the reflectivity of the soil surface significantly $(R^{\mathrm{H}} \approx 0.1)$ but not as much as the longitudinal furrows. The measurements of the plane surface at $p = \mathrm{V}$ yielded values $0.02 \leq R^{\mathrm{V}} \leq 0.03$. Longitudinal furrows $(R^{\mathrm{V}} \approx 0.02)$ slightly decreased R^{V} with respect to the plane surface reflectivity, whereas transverse furrows $(R^{\mathrm{V}} \approx 0.04)$ slightly increased R^{V}. The generally low values of R^{V} are due to the fact that the observation angle $\theta = 50^\circ$ was only slightly below the Brewster angle, which is $\theta_{\mathrm{B}} = \arctan\sqrt{|\varepsilon|} \approx 59^\circ$ for the observed $wc = 0.014\ \mathrm{m}^3 \cdot \mathrm{m}^{-3}$.

The modeled reflectivities at $p = \mathrm{H}$ showed the same pattern as the measured reflectivities: R^{H} modeled for the plane surfaces was higher than R^{H} computed for the surface with transverse furrows, which, in turn, exceeded R^{H} computed for the surface with longitudinal furrows. For all surfaces, however, the modeled R^{H} overestimated the measurements by 0.02 to 0.03. At V-polarization, the modeled R^{V} also deviated from the measurements while still showing the same sequence with different topographies as the measured R^{V}. In this case, however, the measurements were underestimated by the model by 0.01 to 0.02.

2) Moist-Soil Measurements [Fig. 4(b)]: The reflectivities R^p measured for the plane moist-soil surfaces decreased in the course of the day from 0.27 to 0.22 at $p = \mathrm{H}$ and from 0.07 to 0.06 at $p = \mathrm{V}$. The decrease is attributed to the drying of the soil surface due to solar radiation and wind. Drying was observed visibly, particularly during the last two measurements (transverse furrows and plane surface), and was also partially noticeable in the wc measured. However, the reflectivity decrease associated with surface drying was quite small in comparison with the influence of the furrows. At H-polarization, the R^{H} of both furrowed surfaces was substantially lower than the R^{H} measured for the plane surface ($R^{\mathrm{H}} \approx 0.13$ for longitudinal furrows and $R^{\mathrm{H}} \approx 0.11$ for transverse furrows). At V-polarization, in contrast, longitudinal furrows led to smaller reflectivity $(R^{\mathrm{V}} \approx 0.04)$ and transverse furrows led to slightly larger reflectivity $(R^{\mathrm{V}} \approx 0.07)$ compared to the adjacent measurements of the plane surface.

The modeled R^p values displayed the same pattern as the measurements, but they generally over- $(p = \mathrm{H})$ or underestimated $(p = \mathrm{V})$ the measured R^p, respectively, similar to what was observed for the dry-soil surface. The deviations between model results and measurements were in the same range as for the dry soil (0.02–0.04 for $p = \mathrm{H}$; 0.01–0.02 for $p = \mathrm{V}$), except for the R^{H} of the moist-soil surface with transverse furrows. Here, an exceptionally high deviation (0.08) between the measured and modeled R^{H}'s was observed (whereas the value measured for the moist-soil surface was only marginally larger than the corresponding R^{H} measured for the dry-soil surface). Generally, however, it can be stated that moist furrows affected R^p similar to the dry ones, whereas the R^p's of all moist surfaces were higher than the R^p's of the corresponding dry-soil surfaces.

B. Relative Reflectivity Changes

The relatively constant offsets that we observed between the measured and the modeled reflectivity values are mainly attributed to a combination of the different effects mentioned in Section III-D. One important factor is that the reflectivity model does not take into account small-scale surface roughness which is, in reality, superimposed on the prepared surfaces, as well as the small-scale heterogeneity of the top soil layer caused by the manipulation of the surface. Another cause for the discrepancies observed might be the assumption in the reflectivity model that soil moisture is constant with depth. Simulations, performed with a coherent radiative-transfer model for layered dielectric media [36] for hypothetical soil moisture profiles, indicated that the observed discrepancies could, to some degree, be errors introduced through this assumption. However, this effect cannot be quantified accurately since the exact soil moisture profile is not known.

Given the observed deviations, it seems expedient to refer to the relative reflectivity changes δR^p, which were caused by the

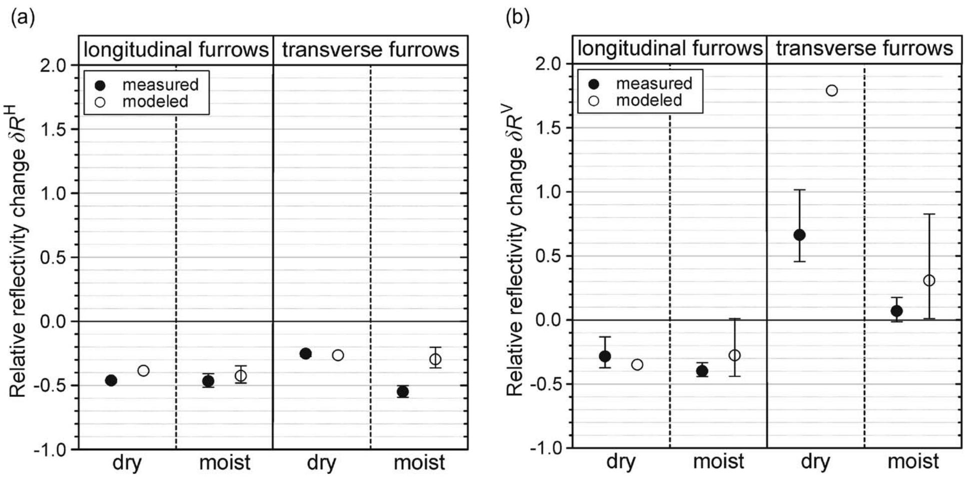

Fig. 5. Relative reflectivity changes δR^p $(p = \mathrm{H, V})$ caused by the furrows under dry- and moist-soil conditions at (a) horizontal and (b) vertical polarization. δR^p's due to longitudinal furrows are shown in the left half of each panel, and δR^p's due to transverse furrows are shown in the right half. Solid symbols are δR^p's calculated from the reflectivities measured, and empty symbols are δR^p's calculated from the reflectivities modeled; both of which are shown in Fig. 4.

furrows (in comparison to the plane surface reflectivities), when discussing the effects of the furrows on the soil reflectivity

$$\delta R^p \equiv \left(R^p_{\mathrm{furrow}} - R^p_{\mathrm{plane}}\right) / R^p_{\mathrm{plane}}. \tag{6}$$

This definition of δR^p (where $p = \mathrm{H, V}$ as before) is the relative difference between the reflectivity R^p_{furrow} of a furrowed surface and the reflectivity R^p_{plane} of the corresponding plane surface. Consequently, the ratio (6) is much less vulnerable to the effects discussed previously, and additionally, the influences of errors introduced through the assumption of a fixed observation angle and of uncertainties in the effective soil temperature T_s are strongly reduced. Therefore, it can be expected that the values of δR^p derived from the modeled and measured R^p are directly comparable and thus suitable for analyzing the effects of the furrows on soil reflectivity.

Fig. 5 shows δR^p calculated with (6) from the reflectivities presented in Fig. 4. Solid symbols refer to δR^p calculated from the measured reflectivities (using the mean R^p_{plane} of the dry- and moist-soil measurements), together with the corresponding uncertainty ranges due to the decrease of R^p_{plane} in the course of the respective day. Empty symbols refer to δR^p derived from the modeled reflectivities (Section III-B). The soil permittivity ε used as input to the reflectivity model was computed from the *in situ* soil-water content wc using (3). In doing so, R^p_{furrow}'s were modeled with the wc observed during the respective brightness temperature measurements, and R^p_{plane}'s were calculated either with the mean wc (symbols) or with the highest and lowest wc of the day of measurements (error bars).

Furrows reduced reflectivities at horizontal polarization substantially [Fig. 5(a)]. This is illustrated by the fact that $\delta R^{\mathrm{H}} < 0$ under both dry and moist conditions and for both furrow directions. The modeled and measured δR^{H}'s caused by the longitudinal furrows (left panel) were in the range of $-0.47 \leq \delta R^{\mathrm{H}} \leq -0.39$. This means that longitudinal furrows reduced the reflectivity of the soil surface by almost half compared to $R^{\mathrm{H}}_{\mathrm{plane}}$, whereas no significant differences between dry- and moist-soil conditions were observed. The reflectivity decrease caused by the transverse furrows (right panel) was somewhat smaller. For dry soil, the measurements and model results both yielded $\delta R^{\mathrm{H}} \approx -0.25$, i.e., $R^{\mathrm{H}}_{\mathrm{furrow}}$ was reduced by ≈25% compared to $R^{\mathrm{H}}_{\mathrm{plane}}$. For the moist-soil surface, the δR^{H}'s measured and modeled deviate from each other. The model predicted approximately the same value as that for dry soil ($\delta R^{\mathrm{H}} \approx -0.3$), whereas the value measured dropped to $\delta R^{\mathrm{H}} \approx -0.55$. This is a consequence of the discrepancy of 0.08 between the measured and modeled R^{H}'s for the moist-soil surface with transverse furrows (see Fig. 4). The strikingly low value for R^{H} measured cannot be explained conclusively. However, it is assumed that this was not solely caused by the transverse furrows but rather is a combination of different effects. Possibly, the drying of the uppermost soil layer observed during the day led to a dielectric profile with distinct layering, causing coherent effects which, in turn, affected R^{H}. Furthermore, an agglomeration of soil particles near the surface was observed in the course of the day, which may also have influenced the measurements. For these reasons, the R^{H} measured for the moist-soil surface with transverse furrows will be excluded from the further analysis described in Section IV-C.

At vertical polarization [Fig. 5(b)], the relative reflectivity changes δR^{V} caused by the furrows show a more diverse pattern. The measured and modeled δR^{V}'s for longitudinal furrows (left panel) are in the range $-0.39 \leq \delta R^{\mathrm{V}} \leq -0.28$, and it is not possible to detect a clear correlation with soil moisture wc. The measurements suggest that δR^{V} decreases slightly with increasing wc, whereas the model indicates a small increase. In contrast, the δR^{V} caused by the transverse furrows (right panel) is strongly dependent on wc. Changing the surface topography from plane to transverse furrows caused the measured reflectivities to increase substantially when the soil surface was dry ($\delta R^{\mathrm{V}} \approx 0.66$), but only a small change was observed under moist conditions ($\delta R^{\mathrm{V}} \approx 0.07$). The corresponding modeled reflectivities show the same trend with soil moisture, whereas the magnitude of the δR^{V} was significantly higher for dry soil ($\delta R^{\mathrm{V}} \approx 1.79$) and somewhat larger for moist soil ($\delta R^{\mathrm{V}} \approx 0.31$). It is striking that both the modeled and the measured δR^{V}'s for transverse furrows were > 0 and that they were larger for dry than for moist soil even when the

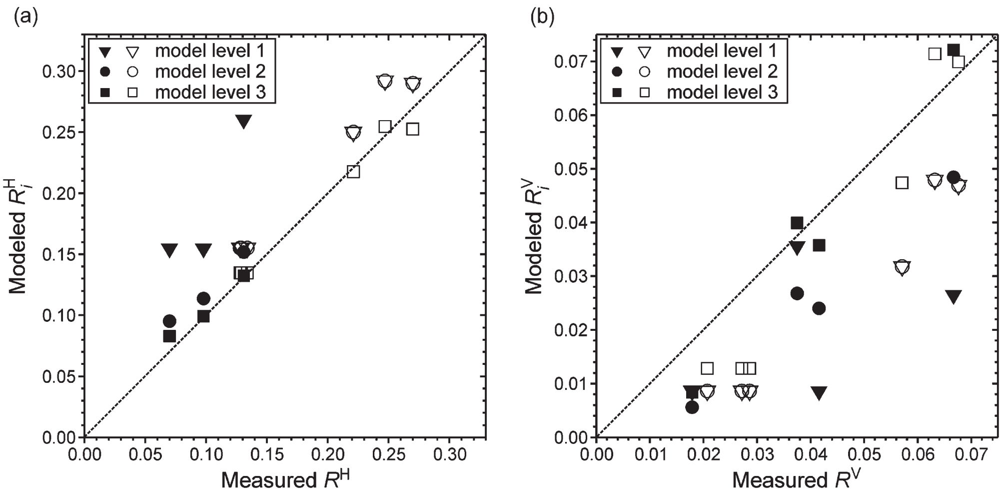

Fig. 6. Scatter plots of measured versus modeled reflectivities (R^p, R_i^p) for the three model levels $i = 1$ (triangles), 2 (circles), and 3 (squares) for (a) horizontal and (b) vertical polarization (see text for the explanation of the different model levels). Empty symbols are for plane surfaces. Solid symbols are for furrowed surfaces. The dashed line is the 1 : 1 line.

uncertainties of δR^V, arising from the uncertainties in wc, are considered. It allows drawing the conclusion that reflectivities at vertical polarization may be increased as a result of polarization crosstalk effects which can change a horizontally or vertically polarized electromagnetic wave into an elliptically polarized wave. Similar effects are also predicted by the integral equation model (IEM) [37] when used to compute reflectivities of random rough surfaces. For dry soil, this effect is even greater, as the emission depth increases, which promotes volume scattering and hence leads to depolarization of the radiance.

The overestimation of δR^V by the model can partly be explained by uncertainties in the observation angle θ. For experimental reasons, the main direction of the antenna can differ somewhat from the aspired value $\theta = 50^\circ$ that was used in the reflectivity model. Furthermore, the local observation angles are slightly different from θ for regions on the soil surface which are not exactly at the intersection with the antenna's main direction. Varying θ by $\pm 3^\circ$ when calculating δR^p resulted in significant changes of δR^V due to transverse furrows under dry- $(0.95 \leq \delta R^V \leq 4.11)$ and moist-soil conditions $(0.12 \leq \delta R^V \leq 0.64)$, whereas for all other cases investigated, the resulting uncertainties in δR^p were ≤ 0.1. Furthermore, the overestimation of δR^V due to the transverse furrows by the model can also be an indication that polarization crosstalk is overrated by the reflectivity model that we used. Similar discrepancies were observed in [34] when calculating rough-surface reflectivities with the IEM [37].

C. Model Performance

As we have shown previously, the physical reflectivity model was able to reproduce reasonably well the observed dependence of soil reflectivity on furrow orientation and soil moisture. However, when the measured and modeled reflectivities R^p $(p = \mathrm{H, V})$ were compared directly, rather than comparing the relative reflectivity changes δR^p, the modeled values differed from the observations. These deviations are ascribed mainly to the small-scale surface roughness superimposed on the furrows and the heterogeneity of the soil surface layer due to drying and the manipulation of the soil surface. Additional sources of error are the assumption of a fixed observation angle and a constant soil moisture profile with soil depth, as well as our approximation for the effective ground temperature. To further improve the agreement between measurements and simulations, we used the empirical approach described in Section III-D. Thereby, the reflectivities calculated with the physical reflectivity model were adapted to the observations with (4) using the parameter values $h^H = 0.137$ and $h^V = -0.399$. These values for h^p for the best agreement between the measurements and the model results were found by minimizing the cost function (5).

To illustrate the model performance, a scatter plot with the measured and modeled reflectivities for three different model levels i is shown in Fig. 6. The measured reflectivities R^p (plotted along the X-axis) are identical to the reflectivities indicated by the solid symbols in Fig. 4. They are opposed to the modeled reflectivities R_i^p $(i = 1, 2, 3)$ (plotted along the Y-axis), which are as follows.

1) R_1^p's were simply modeled with the Fresnel equations regardless of whether the surface was plane or furrowed. The corresponding tuples (R^p, R_1^p) are shown as triangles in Fig. 6.
2) R_2^p's were calculated with the reflectivity model for periodic surfaces described in Section III-B. The model distinguishes between the different soil topographies: plane surface, longitudinal furrows, and transverse furrows. R_2^p's are identical to the modeled reflectivities presented in Fig. 4. The corresponding tuples (R^p, R_2^p) are shown as circles in Fig. 6.
3) R_3^p's are reflectivities derived from R_2^p using the empirical correction described in Section III-D. The corresponding tuples (R^p, R_3^p) are shown as squares in Fig. 6.

As expected, using the Fresnel equations results in a poor agreement between measurements R^p and model simulations R_1^p (triangles). The root-mean-square differences (residua) between R^p and R_1^p are 0.0549 for $p = \mathrm{H}$ and 0.0176 for $p = \mathrm{V}$ (Table I). The large residua are mainly caused by the

TABLE I
ROOT-MEAN-SQUARE DIFFERENCES (RESIDUA) BETWEEN THE MEASURED R^p AND MODELED R_i^p FOR THE THREE DIFFERENT MODEL LEVELS $i = 1, 2, 3$ SHOWN IN FIG. 6

model level i		residua	
		$p = \mathrm{H}$	$p = \mathrm{V}$
1	Fresnel equations	0.0549	0.0176
2	reflectivity model (Section III-B)	0.0089	0.0056
3	reflectivity model + empirical correction	0.0028	0.0029

considerable discrepancies between the reflectivities measured for the furrowed surfaces and those modeled (solid triangles).

Using the reflectivity model for periodic surfaces yields, for the plane surfaces, the same reflectivities $R_2^p = R_1^p$ as the calculations with the Fresnel equations (empty circles). For the furrowed surfaces (solid circles), however, R_2^p deviates considerably from R_1^p, resulting in a much better agreement between the measurements and simulations. This manifests itself in the considerably reduced residua of 0.0089 for $p = \mathrm{H}$ and 0.0056 for $p = \mathrm{V}$ (Table I). However, at horizontal polarization, the modeled reflectivity still overestimates the measurements ($R_2^{\mathrm{H}} > R^{\mathrm{H}}$), while at vertical polarization, the model underestimates the observations ($R_2^{\mathrm{V}} < R^{\mathrm{V}}$).

Using the correction presented in Section III-D results in a further improvement of the model performance (squares). At $p = \mathrm{H}$, the modeled R_3^{H} values are in very good agreement with the measured R^{H}, resulting in a residuum of 0.0028. At $p = \mathrm{V}$, the improvement was not as striking, but here as well, the resulting data tuples $(R^{\mathrm{V}}, R_3^{\mathrm{V}})$ were moved toward the $1:1$ line, and the residuum was further reduced to 0.0029.

V. CONCLUSION

We found that furrows had a distinct impact on the observed soil reflectivities at both polarizations and for both furrow directions investigated. At horizontal polarization, furrows generally reduced the reflectivity ($\delta R^{\mathrm{H}} < 0$). The relative change δR^{H} with respect to the plane surface reflectivity was more pronounced for longitudinal furrows than for transverse furrows, and no significant dependence of δR^{H} on soil moisture was observed. At vertical polarization, the reflectivity of the soil was reduced by the longitudinal furrows ($\delta R^{\mathrm{V}} < 0$) with no clear dependence of δR^{V} on soil moisture. In contrast to that, transverse furrows led to an increase in the soil reflectivity ($\delta R^{\mathrm{V}} > 0$), which, however, showed a strong dependence on soil moisture. These results demonstrate the importance of considering the adequate soil topography when retrieving geophysical parameters from L-band signatures emitted from a furrowed soil surface.

The model simulations performed illustrate that this can be achieved by choosing an appropriate reflectivity model. When reflectivities were computed with the physical reflectivity model that takes into account the periodic soil topography, the residua between the measured and modeled reflectivities were reduced by a factor of ≈ 6 ($p = \mathrm{H}$) and ≈ 3 ($p = \mathrm{V}$), respectively, in comparison with the residua obtained by using the Fresnel equations (Table I). The agreement between the measured and modeled reflectivities was further improved by additionally applying a simple empirical correction to account for the small-scale heterogeneity of the top soil layer. This reduced the residua again by a factor of ≈ 3 ($p = \mathrm{H}$) and ≈ 2 ($p = \mathrm{V}$), respectively (Table I).

The knowledge gained in this study is useful for estimating the implications of periodic soil topography with dimensions in the range of the observation wavelength on soil moisture retrievals, e.g., from SMOS or airborne radiometer measurements over agricultural areas. In addition, the findings can be used to identify such particular surface patterns on the basis of the brightness temperatures measured.

ACKNOWLEDGMENT

The authors would like to thank H.-R. Benedickter and F. Hüsler for performing the soil permittivity measurements, M. Nitsche for helping preparing the furrowed soil surfaces, and M. Stähli for the helpful comments on the manuscript. The authors would also like to thank S. Dingwall for the editorial work on the manuscript.

REFERENCES

[1] T. Schmugge, "Remote sensing of soil moisture," in *Encyclopedia of Hydrological Forecasting*, M. G. Anderson and T. Burt, Eds. Chichester, U.K.: Wiley, 1985, pp. 101–124.

[2] A. M. Shutko, "Microwave radiometry of lands under natural and artificial moistening," *IEEE Trans. Geosci. Remote Sens.*, vol. GRS-20, no. 1, pp. 18–26, Jan. 1982.

[3] Y. H. Kerr, P. Waldteufel, J. P. Wigneron, S. Delwart, F. Cabot, J. Boutin, M. J. Escorihuela, J. Font, N. Reul, C. Gruhier, S. E. Juglea, M. R. Drinkwater, A. Hahne, M. Martin-Neira, and S. Mecklenburg, "The SMOS mission: New tool for monitoring key elements of the global water cycle," *Proc. IEEE*, vol. 98, no. 5, pp. 666–687, May 2010.

[4] J.-P. Wigneron, Y. Kerr, P. Waldteufel, K. Saleh, M.-J. Escorihuela, P. Richaume, P. Ferrazzoli, P. de Rosnay, R. Gurney, J.-C. Calvet, J. P. Grant, M. Guglielmetti, B. Hornbuckle, C. Mätzler, T. Pellarin, and M. Schwank, "L-band microwave emission of the biosphere (L-MEB) model: Description and calibration against experimental data sets over crop fields," *Remote Sens. Environ.*, vol. 107, no. 4, pp. 639–655, Apr. 2007.

[5] K. Saleh, Y. H. Kerr, G. Boulet, P. Maisongrande, P. de Rosnay, D. Floricioiu, M. J. Escorihuela, J.-P. Wigneron, A. Cano, E. López-Baeza, J. P. Grant, J. Balling, N. Skou, M. Berger, S. Delwart, P. Wursteisen, P. Panciera, and J. P. Walker, "The CoSMOS L-band experiment in Southeast Australia," in *Proc. IEEE IGARSS*, 2007, pp. 3948–3951.

[6] B. J. Choudhury, T. J. Schmugge, A. Chang, and R. W. Newton, "Effect of surface roughness on the microwave emission from soil," *J. Geophys. Res.*, vol. 84, no. C9, pp. 5699–5706, 1979.

[7] M. J. Escorihuela, Y. H. Kerr, P. de Rosnay, J.-P. Wigneron, J.-C. Calvet, and F. Lemaître, "A simple model of the bare soil microwave emission at L-band," *IEEE Trans. Geosci. Remote Sens.*, vol. 45, no. 7, pp. 1978–1987, Jul. 2007.

[8] T. Mo and T. J. Schmugge, "A parameterization of the effect of surface roughness on microwave emission," *IEEE Trans. Geosci. Remote Sens.*, vol. GRS-25, no. 4, pp. 481–486, Jul. 1987.

[9] J.-P. Wigneron, L. Laguerre, and Y. H. Kerr, "A simple parameterization of the L-band microwave emission from rough agricultural soils," *IEEE Trans. Geosci. Remote Sens.*, vol. 39, no. 8, pp. 1697–1707, Aug. 2001.

[10] S. Paloscia, P. Pampaloni, L. Chiarantini, S. Coppo, S. Gagliani, and G. Luzi, "Multifrequency passive microwave remote sensing of soil moisture and roughness," *Int. J. Remote Sens.*, vol. 14, no. 3, pp. 467–483, Feb. 1993.

[11] J. R. Wang, R. W. Newton, and J. W. Rouse, "Passive microwave remote sensing of soil moisture: The effect of tilled row structure," *IEEE Trans. Geosci. Remote Sens.*, vol. GRS-18, no. 4, pp. 296–302, Oct. 1980.

[12] X. Yin, Y. Liu, and H. Zhang, "Removing the impact of wind direction on remote sensing of sea surface salinity," *Chin. Sci. Bull.*, vol. 51, no. 11, pp. 1368–1373, Jun. 2006.

[13] O. Isoguchi and M. Shimada, "Preliminary study on developing an L-band wind retrieval model function using ALOS/PALSAR," presented at the Envisat Symp., Montreux, Switzerland, Jul. 2007, ESA SP-636.
[14] L. Tsang, J. A. Kong, and K.-H. Ding, *Scattering of Electromagnetic Waves: Theories and Applications*, vol. 1. New York: Wiley, 2000.
[15] L. Tsang, J. A. Kong, K.-H. Ding, and C. O. Ao, *Scattering of Electromagnetic Waves: Numerical Simulations*, vol. 2. New York: Wiley, 2001.
[16] C. Mätzler, D. Weber, M. Wüthrich, K. Schneeberger, C. Stamm, and H. Flühler, "ELBARA, the ETH L-band radiometer for soil moisture research," in *Proc. IEEE IGARSS*, Toulouse, France, 2003, pp. 3058–3060.
[17] W. Gerwin, W. Schaaf, D. Biemelt, A. Fischer, S. Winter, and R. F. Hüttl, "The artificial catchment "Chicken Creek" (Lusatia, Germany)—A landscape laboratory for interdisciplinary studies of initial ecosystem development," *Ecol. Eng.*, vol. 35, no. 12, pp. 1786–1796, Dec. 2009.
[18] H. M. Picket, J. C. Hardy, and J. Farhoomand, "Characterization of a dual-mode horn for submillimeter wavelengths," *IEEE Trans. Microw. Theory Tech.*, vol. MTT-32, no. 8, pp. 936–937, Aug. 1984.
[19] M. Guglielmetti, M. Schwank, C. Mätzler, C. Oberdörster, J. Vanderborght, and H. Flühler, "FOSMEX: Forest soil moisture experiments with microwave radiometry," *IEEE Trans. Geosci. Remote Sens.*, vol. 46, no. 3, pp. 727–735, Mar. 2008.
[20] M. Guglielmetti, M. Schwank, C. Mätzler, C. Oberdörster, J. Vanderborght, and H. Flühler, "Measured microwave radiative transfer properties of a deciduous forest canopy," *Remote Sens. Environ.*, vol. 109, no. 4, pp. 523–532, Aug. 2007.
[21] K. Schneeberger, M. Schwank, C. Stamm, P. de Rosnay, C. Mätzler, and H. Flühler, "Topsoil structure influencing soil water retrieval by microwave radiometry," *Vadose Zone J.*, vol. 3, no. 4, pp. 1169–1179, Nov. 2004.
[22] M. Schwank, M. Guglielmetti, C. Mätzler, and H. Flühler, "Testing a new model for the L-band radiation of moist leaf litter," *IEEE Trans. Geosci. Remote Sens.*, vol. 46, no. 7, pp. 1982–1994, Jul. 2008.
[23] M. Schwank and C. Mätzler, "L-band radiometer measurements of soil water under growing clover grass," *IEEE Trans. Geosci. Remote Sens.*, vol. 43, no. 10, pp. 2225–2237, Oct. 2005.
[24] M. Schwank, M. Stähli, H. Wydler, J. Leuenberger, C. Mätzler, and H. Flühler, "Microwave L-band emission of freezing soil," *IEEE Trans. Geosci. Remote Sens.*, vol. 42, no. 6, pp. 1252–1261, Jun. 2004.
[25] I. Völksch, M. Schwank, and C. Mätzler, "L-band reflectivity of a wire grid above a dielectric surface," *IEEE Geosci. Remote Sens. Lett.*, vol. 7, no. 3, pp. 601–605, Jul. 2010.
[26] T. Pellarin, J.-P. Wigneron, J.-C. Calvet, M. Berger, H. Douville, P. Ferrazzoli, Y. H. Kerr, E. Lopez-Baeza, J. Pulliainen, L. P. Simmonds, and P. Waldteufel, "Two-year global simulation of L-band brightness temperatures over land," *IEEE Trans. Geosci. Remote Sens.*, vol. 41, no. 9, pp. 2135–2139, Sep. 2003.
[27] M. Schwank, A. Wiesmann, C. Werner, C. Mätzler, D. Weber, A. Murk, I. Völksch, and U. Wegmüller, "ELBARA II, an L-band radiometer system for soil moisture research," *Sensors*, vol. 10, no. 1, pp. 584–612, 2010.
[28] B. J. Choudhury, T. Schmugge, and T. Mo, "A parameterization of effective soil temperature for microwave emission," *J. Geophys. Res.*, vol. 87, no. C2, pp. 1301–1304, 1982.
[29] G. C. Topp, J. L. Davis, and A. P. Annan, "Electromagnetic determination of soil water content: Measurements in coaxial transmission lines," *Water Resour. Res.*, vol. 16, no. 3, pp. 574–582, 1980.
[30] M. C. Dobson, F. T. Ulaby, M. T. Hallikainen, and M. A. El-Rayes, "Microwave dielectric behaviour of wet soil: Part II—Dielectric mixing models," *IEEE Trans. Geosci. Remote Sens.*, vol. 23, no. 1, pp. 35–46, Jan. 1985.
[31] V. L. Mironov, L. G. Kosolapova, and S. V. Fomin, "Physically and mineralogically based spectroscopic dielectric model for moist soils," *IEEE Trans. Geosci. Remote Sens.*, vol. 47, no. 7, pp. 2059–2070, Jul. 2009.
[32] J. R. Wang and B. J. Choudhury, "Remote sensing of soil moisture content over bare field at 1.4 GHz frequency," *J. Geophys. Res.*, vol. 86, no. C6, pp. 5277–5282, 1981.
[33] E. G. Njoku, T. J. Jackson, V. Lakshmi, T. K. Chan, and S. V. Nghiem, "Soil moisture retrieval from AMSR-E," *IEEE Trans. Geosci. Remote Sens.*, vol. 41, no. 2, pp. 215–229, Feb. 2003.
[34] M. Schwank, I. Völksch, J.-P. Wigneron, Y. H. Kerr, A. Mialon, P. de Rosnay, and C. Mätzler, "Comparison of two bare-soil reflectivity models and validation with L-band radiometer measurements," *IEEE Trans. Geosci. Remote Sens.*, vol. 48, no. 1, pp. 325–337, Jan. 2010.
[35] J. Shi, K. S. Chen, Q. Li, T. Jackson, P. E. O'Neill, and L. Tsang, "A parameterized surface reflectivity model and estimation of bare-surface soil moisture with L-band radiometer," *IEEE Trans. Geosci. Remote Sens.*, vol. 40, no. 12, pp. 2674–2686, Dec. 2002.
[36] J. A. Dobrowolski, "Optical properties of films and coatings," in *Handbook of Optics*, vol. I, M. Bass, E. W. van Stryland, D. R. Wiliams, and W. L. Wolfe, Eds. New York: McGraw-Hill, 1995, pp. 42.1–42.130.
[37] A. K. Fung, *Microwave Scattering and Emission Models and Their Application*. Boston, MA: Artech House, 1994.

Ingo Völksch received the B.S. degree in geology from the Friedrich Schiller University of Jena, Jena, Germany, and the M.S. degree in earth sciences with a special focus on glaciology from the Swiss Federal Institute of Technology (ETH) Zürich, Zürich, Switzerland, in 2004, with his thesis entitled "Monitoring and modeling of small-scale spatial variations of mountain permafrost properties." In the following year, he gained further experience in permafrost modeling and snow hydrology, working as a Research Assistant with the Swiss Federal Institute of Snow and Avalanche Research (SLF), Davos, Switzerland. He then turned his focus toward passive microwave radiometry and is currently working toward the Ph.D. degree in the mountain hydrology group of the WSL Swiss Federal Institute for Forest, Snow and Landscape Research, Birmensdorf, Switzerland. His work focuses on L-band signatures of soils with oriented surface structures.

Mike Schwank received the Ph.D. degree in physics from the Swiss Federal Institute of Technology (ETH) Zürich, Zürich, Switzerland, in 1999. The topic of his Ph.D. thesis was "Nanolithography using a high-pressure scanning-tunneling microscope."

In the following three years, he gained experience in the industrial environment, where he was a Research and Development Engineer in the field of micro-optics. From 2003 to 2010, he was working in the research field of microwave remote sensing applied to soil moisture detection as a Senior Research Assistant first with the Institute of Terrestrial Ecology, ETH Zürich, and then with the WSL Swiss Federal Institute for Forest, Snow and Landscape Research, Birmensdorf, Switzerland. His research involved practical and theoretical aspects of microwave radiometry. In addition to his research at WSL, he was also with Gamma Remote Sensing Research and Consulting AG, Gümligen, Switzerland, where he was involved in the production of microwave radiometers to be deployed for ground-based Soil Moisture and Ocean Salinity calibration/validation purposes. Since August 2010, he has been with the German Research Centre for Geosciences (GFZ), Potsdam, Germany, where he is in charge of the coordination of the Northeastern German Lowland Observatory, which is one of the four Terrestrial Environmental Observatories.

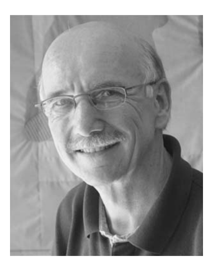

Christian Mätzler (M'96–SM'03) studied physics at the University of Bern, Bern, Switzerland, with minors in mathematics and geography, where he received the M.Sc. degree in 1970, the Ph.D. degree in solar radio astronomy in 1974, and the Habilitation in applied physics with emphasis on remote sensing methods in 1986.

After postdoctoral research with the Goddard Space Flight Center, National Aeronautics and Space Administration, Greenbelt, MD, and with the Swiss Federal Institute of Technology (ETH) Zürich, Zürich, Switzerland, he returned to the Institute of Applied Physics, University of Bern, in 1978 as a Research Group Leader for terrestrial and atmospheric radiometry and remote sensing. He received the title of Titular Professor in applied physics and remote sensing in 1992. He spent sabbaticals in 1996 at the University of Colorado, Denver, and the University of Washington, Seattle, and in 2004 at the Paris Observatory, Paris, France. In July 2010, he went into retirement. His studies have been concentrated on microwave (1–100 GHz) signatures for active and passive remote sensing of the atmosphere, snow, ice, soil, and vegetation, as well as the development of methods for dielectric and propagation measurements for such media, while complementary work has been done in his group at infrared and optical wavelengths. He is the Editor of a book on thermal microwave emission with applications for remote sensing. He is interested in understanding the observed processes and in the interactions between surface and atmosphere. Based on the experimental work, he has contributed to the development of radiative-transfer models, on methods for retrieving geophysical parameters from microwave remote sensors, and on the assessment of optimum sensor parameters.